Large AuAg Alloy Nanoparticles Synthesized in Organic Media Using a One-Pot Reaction: Their Applications for High-Performance Bulk Heterojunction Solar Cells

Hsieh-Chih Chen, Shang-Wei Chou, Wei-Hsuan Tseng, I-Wen P. Chen, Chi-Chang Liu, Chun Liu, Chien-Liang Liu, Chun-hsien Chen, Chih-I Wu,* and Pi-Tai Chou**

A one-pot synthesis of large size and high quality AuAg alloy nanoparticles (NPs) with well controlled compositions via hot organic media is demonstrated. Amid the synthesis, complexation between trioctylphosphine (TOP) and metal precursors is found, which slows down the rate of nucleation and leads to the growth of large-size AuAg nanoalloys. The wavelength and relative intensities of the resulting plasmon bands are readily fine-tuned during the synthetic process using different Au/Ag precursors molar ratios. In the polymer solar cells, a key step in achieving high efficiency is the utilization of 1% $Au_{11}Ag_{89}$ alloy NPs embedded in the active layer to promote the power conversion efficiency (PCE) up to 4.73%, which outperforms the reference device based on the control standard device of poly(3-hexylthiophene) (P3HT):phenyl-C_{61}-butyric acid methyl ester ($PC_{61}BM$) under identical conditions. Corresponding increases in short-circuit current density (J_{sc}), open-circuit voltage (V_{oc}), fill factor (FF), and incident photon-to-current efficiency (IPCE) enable 31% PCE improvement due to the enhancement of the light-trapping and the improvement of charge transport in the active layer. The findings advance the fundamental understanding and point to the superiority of $Au_{11}Ag_{89}$ nanoalloys as a promising metallic additive over Au, Ag, and $Au_{28}Ag_{72}$ alloy NPs to boost the solar cell performance.

1. Introduction

Development of efficient photovoltaic devices comprising polymer solar cells[1–12] and hybrid solar cells[13–16] based on bulk heterojunction (BHJ) configuration has been attracting considerable interest due to their low-cost fabrication, mechanical flexibility and potential to provide efficient conversion of solar energy.[1–16] There are a number of challenges on the way to achieve high power conversion efficiency (PCE) of solar cells. These include the development of low bandgap conjugated polymers with respect to broad light absorption and efficient charge separation/transportation via controlling the nanostructure of active layer. As a result, several highly efficient polymers have been reported with high PCE surpassing than 7% to date.[7–9]

Considering the power conversion processes, including solar light absorption, exciton generation, exciton dissociation, and charge carriers transport, all occur in the active layers.[17–25] Therefore, gaining insight into the nanostructure of the active layer and the corresponding morphology,[22–25] as well as the photovoltaic mechanism,[17–21] is beneficial to meliorate the PCE of the resulting BHJ solar cells. It is well known that reducing recombination is a linchpin of increasing device efficiency.[22] Therefore, decreasing the thickness of the active layer and maximizing its absorption capability to reduce the device resistance and the probability of charge recombination play key roles to improve the device's PCE. From this viewpoint, a remarkable amount of work has been devoted to utilizing metal nanoparticles (NPs) strategies that result from their localized surface plasmon resonance (LSPR) for efficient light trapping in the active layer in an aim to enhance photon absorption without the need for a thick film.[26–28] To date, most studies are focused on single-composition of gold, silver, and copper NPs, which are almost exclusively suspended in aqueous solution.[28–30] In comparison, much less systematic experimental study of alloying metal NPs has been performed in photovoltaic performance so far.[31] More importantly, conjugated polymers are soluble primarily in organic solvents, which are incompatible with aqueous media. This limits the use of these metal NPs in organic photovoltaic devices. Although many of the device geometries have been reported to directly introduce various species of aqueous phase metal NPs in poly(3,4-ethylenedioxythiophene) poly(styrenesulfonate)

Dr. H.-C. Chen, Dr. S.-W. Chou, Dr. I-W. P. Chen, C.-C. Liu, C. Liu, C.-L. Liu, Prof. C.-h. Chen, Prof. P.-T. Chou
Department of Chemistry
National Taiwan University
Taipei 106, Taiwan
E-mail: chhchen@ntu.edu.tw; chop@ntu.edu.tw
Dr. H.-C. Chen, Dr. S.-W. Chou, Prof. C.-h. Chen, Prof. C.-I. Wu, Prof. P.-T. Chou
Center of Emerging Material and Advanced Devices
National Taiwan University
Taipei 106, Taiwan
E-mail: chihiwu@cc.ee.ntu.edu.tw
W.-H. Tseng, Prof. C.-I. Wu
Department of Electrical Engineering and Graduate Institute of Electrooptical Engineering
National Taiwan University
Taipei 106, Taiwan

DOI: 10.1002/adfm.201200218

(PEDOT:PSS) layer,[32,33] the PCEs enhancement is very limited. Because the PEDOT:PSS layer is essentially transparent in the visible and is used as a hole transport buffer layer, increased light absorption may not be an efficient plasmonic enhancement mechanism.

To facilitate solution processing for the fabrication of the efficient photovoltaic devices, metal NPs from aqueous to organic solution has been reported by hydrophobization of the NPs' surface using polymeric ligands, such as polyvinylpyrrolidone (PVP), polyethylene glycol (PEG), and polystyrene-*block*-poly(2-vinyl-pyridine) (PS-*b*-P2VP).[31,34–37] However, there are very few successful reports regarding the transfer of larger spherical NPs (>20 nm) to organic solvents because of the stronger van der Waals forces between the larger NPs. This together with the weaker electrostatic stabilization in organic solvent, results in aggregation. In addition, the bulky polymeric-ligands capped NPs form highly insulating barriers between adjacent NPs, resulting in a high density of surface traps that cause a strong depletion of charge carriers in the active layer. Apart from this approach, direct synthesis of alloy NPs in organic solvents has proven to be more challenging because of the poor dielectric stabilization, as evidenced by the surprisingly small size of monodisperse metal NPs reported by a number of preparations.[38–40] Being small in size (<10 nm), the scattered field decays evanescently away from the NPs, resulting in strong absorption (optical loss) and weak scattering.[41,42] Conversely, bigger NPs can efficiently scatter light, effectively increasing the path length.

Herein, we report for the first time a facile and systematic synthetic protocol for preparation of large size (~20 nm) and highly monodisperse of AuAg alloy NPs by means of one-pot method via hot organic media in the presence of trioctylphosphine (TOP), oleic acid (OAc), and oleylamine (OAm) as stabilizing agents. Taking advantage of their induced LSPR absorption properties, we then apply these as-prepared AuAg nanoalloys, pristine Au and Ag NPs in the photovoltaic devices. Upon optimizing the amount of $Au_{11}Ag_{89}$ nanoalloys doped in poly(3-hexylthiophene) (P3HT):phenyl-C_{61}-butyric acid methyl ester ($PC_{61}BM$) blend, we demonstrate a highly praiseworthy power conversion efficiency (PCE) of 4.73% as compared to that of the control standard device of P3HT:$PC_{61}BM$ (3.61%) fabricated and tested under the same conditions. Detail of synthesis and reaction mechanism of large-size AuAg nanoalloys as well as the device fabrication is elaborated in the following sections.

2. Results and Discussion

2.1. Characterization of AuAg Nanoalloys

The AuAg alloys were synthesized using $AgNO_3$ and $Au(ac)_3$ as the precursors for Ag and Au, respectively, in a one pot reaction under the presence of various stabilizing ligands such as TOP, OAc, and OAm (see Experimental Section), in which TOP plays a key role in controlling the nucleation rate and hence the resulting size of AuAg nanoalloys. It has been well established that upon reaching the supersaturation point, the atoms start to aggregate themselves and become nucleus for the particle growth through the ongoing reduction of precursors.[43] On this basis, studies have pointed out that nucleation rate is a key factor for the size-controlled of NPs.[43–46] The nucleation rate can be controlled by the adjustment of concentration of metal-ligand complexes.[45–47] This strategy follows a sequence of well established rules: 1) the higher concentration of metal-ligand complexes could slow down the nucleation rate; 2) the slow nucleation rate then results in a larger amount of atoms during the particle growth; and 3) the larger amount of atoms is provided to enlarge the particle size during the growth stage. On these bases, particles with larger size are obtained.[45–47] On the contrary, a fewer amount of metal-ligand complexes induced a fast nucleation rate, consequently resulting in small particles.

We successfully applied the above growing mechanism in preparing the required large size of AuAg alloy NPs. Amid the synthesis we found that TOP may complex with the metal precursors at the early stage, leading to slow down the nucleation rate and hence the growth of larger size AuAg alloy NPs. For the clarity of elaboration, **Scheme 1** summarizes the comparative synthetic routes with and without involvement of TOP. The role of TOP played in this synthetic scheme can be evidenced via monitoring the UV-vis spectra (Figure S1a, in Supporting Information). Figure S1a depicts the UV-vis spectra amid the synthesis of AuAg alloy NPs at early stage. Evidently, Ag and AuAg NPs prepared in the presence of TOP reveal distinct absorption band from 310 to 350 nm, whereas there is no characteristic peak at the same region in the absence of TOP. As for a control, no absorption is resolved in the spectral region of interest, i.e. 310–350 nm for the free ligands TOP. Therefore, the presence of TOP ligand seems to interact with the Ag metal precusors by forming a certain type of coordination complex that consequently slows down the rate of nucleation. Upon adding TOP, as shown in Scheme 1a, slow nucleation provides low concentration of seeds consuming the same amount of monomer and results in large NP size comparing with that without TOP (see Scheme 1b). Although the actual structure of the associated complex is pending resolution, synthesis without TOP results in a substantially smaller AuAg alloys, with an average diameter of only 8.21 ± 0.97 nm (see Figure S1b, Supporting Information), than that (~20 nm,

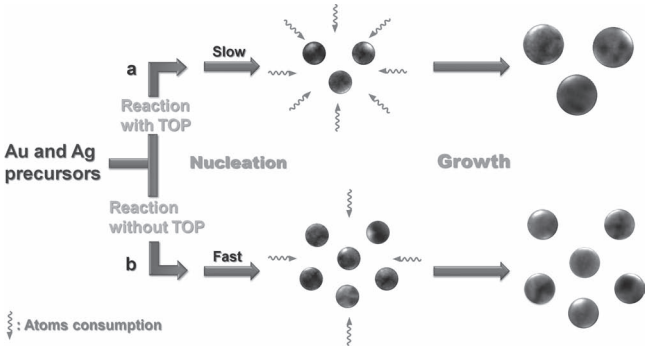

Scheme 1. Schematic routes for the synthesis of the AuAg alloy NPs via TOP ligand-controlled the nucleation rate.

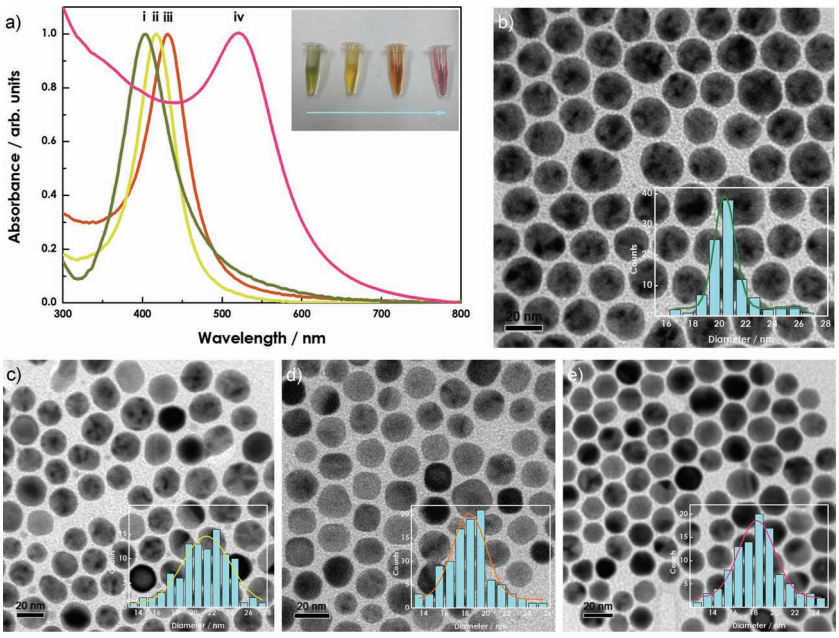

Figure 1. a) Absorption spectra of i) Ag, ii) $Au_{11}Ag_{89}$, iii) $Au_{28}Ag_{72}$, and iv) Au solutions with localized surface plasmon resonance (LSPR) peaks at 404, 418, 432, and 520 nm, respectively. Inset: Photograph (from left to right) of hexane dispersions of Ag, $Au_{11}Ag_{89}$, $Au_{28}Ag_{72}$, and Au showing variation in color. Representative TEM images of b) Ag, c) bimetallic $Au_{11}Ag_{89}$ alloy, d) bimetallic $Au_{28}Ag_{72}$ alloy, and e) Au NPs. Inset: Histograms representing the size distribution of the NPs. The scale bar is 20 nm. The composition of each sample was measured by EDS spectra.

vide infra) of the AuAg alloys with the presence of TOP. Upon varying the stoichiometric ratio for $AgNO_3$ versus $Au(ac)_3$ we then obtained two sets of optimized AuAg alloys in terms of homogeneity (vide infra). The composition of these nanoalloys was then confirmed using an energy-dispersive spectroscopy (EDS) line-scan analysis to identify the elemental profile of the as-prepared NPs. The results shown in Figure S2 of Supporting Information deduce Au/Ag ratios of these bimetallic NPs to be $Au_{11}Ag_{89}$ and $Au_{28}Ag_{72}$, respectively. Additionally, Figure S2c of Supporting Information depicts the tunable plasma bands by using different Au/Ag precursors' molar ratios. Except for slight deviation of the pure Au NPs, the linearity of the plot provides confirmation of alloying.

As shown in the UV-vis absorption spectra (see **Figure 1**a), four as-synthesized metal NPs, namely Au, Ag, $Au_{11}Ag_{89}$, and $Au_{28}Ag_{72}$ dispersed in dilute hexane, all exhibit characteristic plasmon response peaks. The localized surface plasmon resonance (LSPR) peak wavelength (λ_{max}) of Au NPs is located at 520 nm, followed by $Au_{28}Ag_{72}$ nanoalloys at 432nm, $Au_{11}Ag_{89}$ nanoalloys at 418 nm, and Ag NPs at 404 nm. Clearly, as the composition for Ag versus Au increases, a notable blue-shifted of LSPR band is observed, indicating that the plasmon response of the AuAg nanoalloys can be readily fine-tuned by Au/Ag ratio through the hot-organic media reaction.[39,48,49] Figure 1b–e show the TEM images of these bimetallic AuAg NPs, where distinct spherical morphology can be clearly observed. These NPs are good in monodispersity with average diameters of 20.77 ± 2.04 nm for Ag (Figure 1b), 21.47 ± 2.78 nm for $Au_{11}Ag_{89}$ (Figure 1c), 19.8 ± 2.80 nm for $Au_{28}Ag_{72}$ (Figure 1d), and 18.42 ± 2.93 nm for Au NPs (Figure 1e). The high-resolution transmission electron microscopy (HRTEM) image (see Figure S3, Supporting Information) shows a lattice spacing of 0.24 nm, corresponding to the (111) planes of either face-centered cubic (fcc) packed crystal of Au or Ag. It is also noteworthy that the similar lattice constants of Au (4.08 Å) and Ag (4.09 Å) make the resolution of each individual lattice impossible even with HRTEM images. Nevertheless, the formation of nanoalloys with various compositions can be clearly characterized by their corresponding LSPR peak wavelength shown in the absorption spectra (Figure 1a). In this newly developed method, the concentration of Ag-TOP plays a key role for the growth of AuAg nanoalloys with large size. The high Ag-TOP concentration is able to sufficiently suppress the nucleation rate and hence enlarges the final NPs' size. In the Au-rich condition, the low Ag-TOP and high Au atom concentrations result in highly effective nucleation and the formation of NP with relatively smaller size (10 ~ 12 nm). Due to the need of large NPs for enhancing the light scattering effect in PSCs, we therefore select the Ag-rich nanoalloys with particle size of ~20 nm.

2.2. Morphology Studies

The active layer is a crucial part of the BHJ solar cells and the resulting morphology is one of key factors for the performance of solar cells. In this study, the bimetallic $Au_{11}Ag_{89}$ and $Au_{28}Ag_{72}$ NPs were blended into the P3HT:PC_{61}BM (1:1, w/w) system with weight ratios of 1–10%. Tapping mode atomic force microscopy (TM-AFM) topographic studies (**Figure 2**) reveal that the blend films with and without the additive NPs clearly reflect the influence of surface morphology on device performance, since the efficient charge generation and transportation are strongly dependent on the morphology of active layers.[22–25] The plain P3HT:PC_{61}BM (1:1, w/w) film (Figure 2a) possesses uniform and finer phase separation in the blend with a root-mean-square (rms) roughness of 0.672 nm. Such an interpenetrating network in the active layer could facilitate the formation of efficient exciton dissociation interfaces and bicontinuous charge transport channels. In comparison, Figure 2b–d reveal the resulting films with 1–10% $Au_{11}Ag_{89}$ nanoalloys embedded in the polymer matrix. These NPs are nearly spherical and are partially clustered on the surface. The blend film with 1% $Au_{11}Ag_{89}$ alloy NPs shows a relatively smooth surface with a rms roughness of 0.858 nm, indicating uniform dispersion of NPs in the active layer. Nevertheless, upon adding 10 wt% $Au_{11}Ag_{89}$ nanoalloys into the blended film as shown in Figure 2d, the surface of the blend (rms roughness of 1.229 nm) becomes substantially uneven due to the aggregation of alloy NPs, forming a large cluster. The net result is to destroy the interpenetrating pathway for charge transport, resulting in a

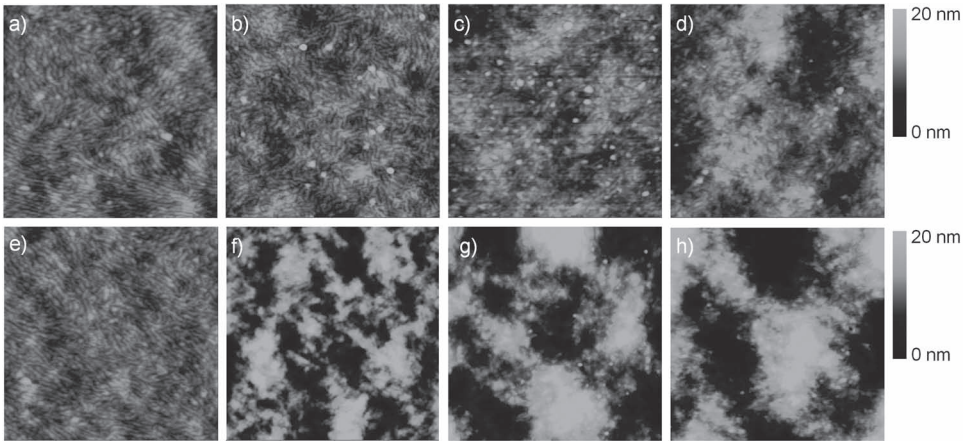

Figure 2. TM-AFM topographic images of P3HT:$PC_{61}BM$ (1:1, w/w) based films blended with $Au_{11}Ag_{89}$ alloy NPs of a) 0%, b) 1%, c) 5%, and d) 10%, as well as blended with $Au_{28}Ag_{72}$ alloy NPs of e) 0%, f) 1%, g) 5%, and h) 10%, respectively. The imaging area is 1 μm × 1 μm.

decrease of device performance (vide infra). Similar phenomenon has also been observed in the Au and Ag nanocluster dispersed in the P3HT:$PC_{61}BM$ blends (see Figure S4, Supporting Information). However, it is interesting to note that the $Au_{28}Ag_{72}$ alloy NPs are obviously not well dispersed in the polymer matrix, and thus tend to significantly aggregate with large-scale phase separation. (Figure 2f–h), even though a lower content of $Au_{28}Ag_{72}$ alloy NPs. Accordingly, the rms roughness for 1%, 5%, and 10% of $Au_{28}Ag_{72}$ nanoalloys in the blends are as high as 2.208, 2.640, and 2.928 nm, respectively. Since the size distribution for $Au_{11}Ag_{89}$ and $Au_{28}Ag_{72}$ is similar, the difference in morphology resulting from NPs sizes may be eliminated. On the other hand, different ligand structure surrounding $Au_{11}Ag_{89}$ and $Au_{28}Ag_{72}$ NPs may play certain role to account for the morphology discrepancy. For example, the $Au_{28}Ag_{72}$ alloy may have high tendency of aggregation, resulting in poor intermixing of the blend components. To gain more insight into the origin of the morphological differences, we perform the corresponding Fourier transform infrared (FTIR) measurements (Figure S5, Supporting Information). Clearly, similar IR spectra are observed for Ag, Au, and $Au_{11}Ag_{89}$ NPs. For example, the absorption peaks of the $-CH_2$ stretching are in the range of 2800–3000 cm^{-1}, while the absorption of –NH stretching vibration (OAm) is broad but distinguishable in the range of 3300–3500 cm^{-1}. The result indicates similar passivation condition on the surface of these nanocrystals. Conversely, only the absorptions of $-CH_2$ stretching in the range of 2800–3000 cm^{-1} are observed on the surface of $Au_{28}Ag_{72}$ nanoalloys, supporting the absence of OAm. In this case, the $-CH_2$ peaks are ascribed to other surfactants such as TOP and OAc. Nevertheless, the N-H peak is rather broad and diffusive, which is difficult to be quantified. Therefore, the results cannot unambiguously conclude that the inferior morphology of $Au_{28}Ag_{72}$ nanoalloys is due to the lack of OAm adsorption. Although this issue is still pending resolution, the structure or composition of the ligand shells appears to depend on the core composition and quite likely is responsible for the microstructural differences in the polymer composite. More information about the morphology properties between $Au_{11}Ag_{89}$ and $Au_{28}Ag_{72}$ doped blend film will be given in the section of ultraviolet photoelectron spectroscopy (UPS) studies. Nevertheless, just as expected, the resulting inferior morphologies decreases the phase-separated interfacial areas for efficient exciton dissociation, which would dramatically diminish the solar cell performance described in the following section.

2.3. Photophysical Properties

The UV-vis spectra of P3HT:$PC_{61}BM$ blend films with various concentrations of $Au_{11}Ag_{89}$ alloy NPs show an absorption peak wavelength (λ_{max}) at 513 nm and two prominent shoulder peaks at 550 and 600 nm, assigned to the characteristic absorption of the crystalline π-stacking structure of P3HT (**Figure 3**a).[50] No additional features in the longer wavelength are identified, implying no significant ground-state charge transfer occurs. The P3HT:$PC_{61}BM$ blend films with 1–10 wt% of $Au_{11}Ag_{89}$ nanoalloys alter the optical response greater than the P3HT:$PC_{61}BM$ blend film, implying more photons can be harvested as used in solar cell performance. The photoluminescence spectra (PL) of P3HT:$PC_{61}BM$ blend films with and without nanoalloys are shown in Figure 3b. Considerable enhancement of the PL emission upon increasing nanoalloys' concentrations suggests that, most likely, the presence of the capping insulating surfactants on the NPs' surface could prevent direct contact between the metal NP and the polymer matrix, thus suppressing exciton quenching on the NPs' surface. This could be further supported by the fact that significant changes in surface morphology of the active layers shown in Figure 2a–d. Another possible reason is that excitation of the LSPR increases the degree of light absorption, and thereby enhancing the light excitation rate, i.e. the increase of the transition moment.

Figure 4a reveals the diffuse reflectance spectra of the devices fabricated with and without $Au_{11}Ag_{89}$ alloy NPs in P3HT:$PC_{61}BM$ blends. This is an important feature in that nanoalloys drastically reduce the reflection over a wide range of wavelengths due to the efficient light scattering in the active layer. To further address the exciton lifetimes and charge

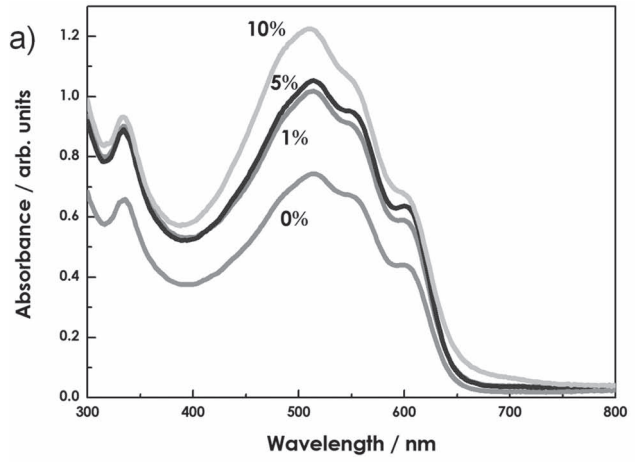

Figure 3. a) UV-vis spectra of P3HT:$PC_{61}BM$ (1:1 by weight) blend films with various concentration of $Au_{11}Ag_{89}$ alloy NPs. b) Photoluminescence spectra of P3HT:$PC_{61}BM$ blend films with various concentration of $Au_{11}Ag_{89}$ alloy NPs using the excitation wavelength of 490 nm.

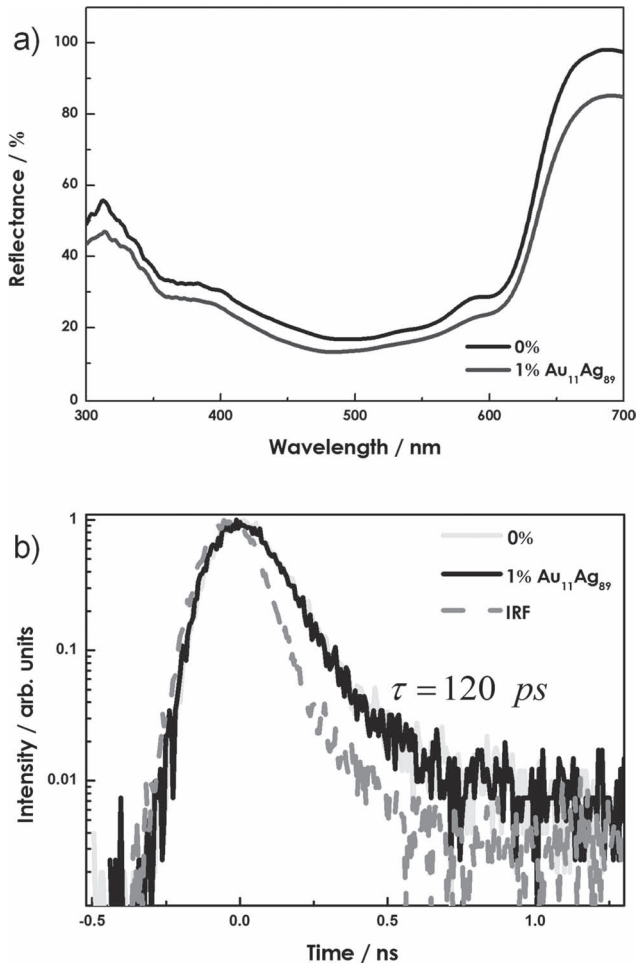

Figure 4. a) Diffuse reflectance spectra of P3HT:$PC_{61}BM$ (1:1 by weight) blend films with (pink color) and without (blue color) the addition of 1 wt% $Au_{11}Ag_{89}$ alloy NPs. b) Time-resolved photoluminance decays monitored at 670 nm for P3HT:$PC_{61}BM$ blend films with and without incorporation of 1% $Au_{11}Ag_{89}$ alloy NPs, along with the instrument response function (IRF) and the excitation wavelength is 400 nm.

carrier dynamics in the active layer with and without AuAg alloy nanoarchitectures, we next investigated their dependence on nanoalloys' concentration by time-correlated single photon counting (TCSPC) technique. The trends in the average lifetime inferred from time-resolved photoluminance measurements are confirmed by the lifetime distributions (see Figure 4b), which not only overlap very well but also are further fitted single-exponentially both with identical lifetimes of ca. 120 ps within experimental error. This might imply that there exists less significant or even negligible enhancement from the excitation of LSPR of the AuAg NPs to boost the probability of exciton dissociation. In other words, the local field enhancement from the narrow band plasmon resonance is not the dominant mechanism for gaining exciton dissociation. Similar emission lifetimes (ca. 120 ps, within experimental error) are also obtained for other blend films upon introducing AuAg nanoalloys with different blend ratios (see Figure S6, Supporting Information). Our TCSPC system typically offers a reliable temporal resolution of ~30 ps after deconvolution. As a result, enhancing the photovoltaic performance of BHJ solar cells with nanoalloys in this study may simply be ascribed to the trivial factor that these alloy NPs can act as an effective optical reflector which causes multiple reflections of light to pass through the active layer several times and therefore effectively increase the light absorption of the solar cells (Figure 3a). This simple point is also well supported by the incident photon-to-current efficiency (IPCE) measurement (vide infra).

2.4. Photovoltaic Performance

BHJ photovoltaic devices were fabricated in a typical configuration of ITO/PEDOT:PSS/P3HT:$PC_{61}BM$:nanoalloys/Ca/Al. The composition ratio of P3HT:$PC_{61}BM$ as an active layer was fixed at 1:1 in weight. Different device fabrication conditions were tested, and the device performance data are summarized in **Table 1**. **Figure 5**a depicts the current density–voltage (J–V) curves of P3HT:$PC_{61}BM$ solar cells with various types of 1%

Table 1. Summary of the fabrication conditions and performance of the BHJ solar cells.

Device[a)]	Type of NPs	NP ratio [wt%]	V_{oc} [V]	J_{sc} [mA cm^{-2}]	FF [%]	PCE [%]
D1	–	0	0.61	10.12	58.4	3.61
D2	Ag	1	0.64	11.96	60.1	4.60
D3	Ag	5	0.63	9.38	55.3	3.27
D4	Ag	10	0.61	8.76	49.8	2.66
D5	$Au_{11}Ag_{89}$	1	0.63	12.21	61.5	4.73
D6	$Au_{11}Ag_{89}$	5	0.63	11.96	61.2	4.61
D7	$Au_{11}Ag_{89}$	10	0.63	11.80	59.4	4.49
D8	$Au_{28}Ag_{72}$	1	0.60	11.38	51.7	3.53
D9	$Au_{28}Ag_{72}$	5	0.57	9.59	41.5	2.27
D10	$Au_{28}Ag_{72}$	10	0.50	8.23	42.3	1.74
D11	Au	1	0.62	11.54	60.6	4.34
D12	Au	5	0.60	9.11	55.5	3.03
D13	Au	10	0.56	7.85	51.8	2.28

[a)] After annealing at 150 °C for 10 min.

NPs under AM 1.5G illumination at 100 mW cm^{-2}. The highest short circuit current density (J_{sc}) of 12.21 mA cm^{-2}, along with an open circuit voltage (V_{oc}) of 0.63 and a high fill factor (FF) of 61.5%, yields an impressive PCE of 4.73% for 1% $Au_{11}Ag_{89}$ nanoalloys in BHJ solar cells. Compared to the reference P3HT:PC_{61}BM device, blending 1% of $Au_{28}Ag_{72}$ alloy in the active layer showed a slightly increased in J_{sc} (11.38 mA cm^{-2}) but simultaneously possessed a poor FF (51.7%), leading to a PCE of 3.53%. Accordingly, the device performance can be pronouncedly improved with introducing small amount of these NPs except of $Au_{28}Ag_{72}$ nanoalloys. The noticeably upward trend in J_{sc} after incorporating the lower NPs concentration suggests that: 1) the efficiency of light harvesting in the polymer blend is greatly improved with incorporation of only a small amount of NPs and 2) the photocurrent generation is not limited by exciton diffusion and/or dissociation in the presence of small amount of NPs. Nevertheless, the results indicate that the superior $Au_{11}Ag_{89}$ nanoalloys are the most promising high-performance metal additive suitable for application in BHJ solar cells.

The devices fabrication conditions for the $Au_{11}Ag_{89}$ NPs were further fine tuned by weight ratio of 0%, 1%, 5%, and 10% with a fixed P3HT:PC_{61}BM loading shown in Figure 5b. Under global solar illumination, the PCE was 3.61% in reference P3HT:PC_{61}BM solar cell with a J_{sc}, a V_{oc}, and a FF of 10.12 mA cm^{-2}, 0.61 V, and 58.4%, respectively. When 1% $Au_{11}Ag_{89}$ alloy NPs were blended with P3HT:PC_{61}BM, the PCE substantially improved to 4.73%, which corresponded to 31% improvement as compared with the reference device. The rapid rise in J_{sc} and FF in the low $Au_{11}Ag_{89}$ concentration suggested that strong light trapping within the active layer. Moreover, the presence of 1% $Au_{11}Ag_{89}$ bimetallic NPs is well mixing with P3HT:PC_{61}BM blend (vide supra), which do not retard the charge separation/transportation. In fact, the competition between light scattering and morphology transition contributed

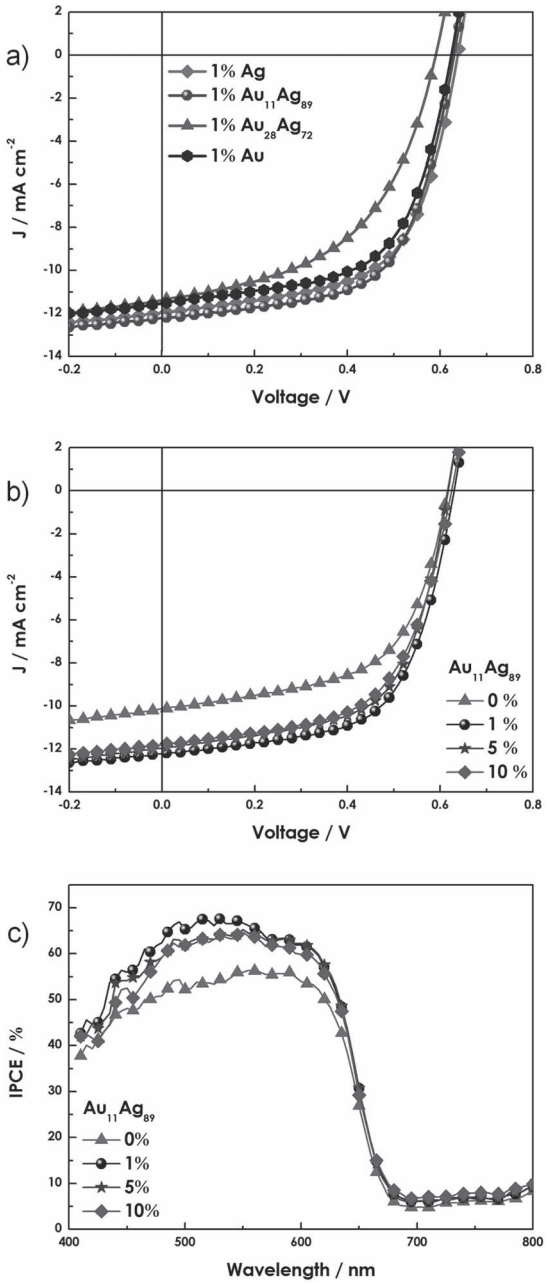

Figure 5. a) Current density–voltage (*J–V*) curves of P3HT:PC_{61}BM (1:1, w/w) based solar cells with 1% Au, $Au_{11}Ag_{89}$, $Au_{28}Ag_{72}$, and Ag NPs under AM1.5G illumination. b) *J–V* characteristics of P3HT:PC_{61}BM devices with $Au_{11}Ag_{89}$ alloy concentration varied from 0% to 10%. c) IPCE spectra of P3HT:PC_{61}BM based solar cells composed of different amount of $Au_{11}Ag_{89}$ nanoalloys.

to the trend in PCE variation (see Table 1). Further increasing the concentration of nanoalloys to 10% had a detrimental effect upon the device performance with a J_{sc} of 11.8 mA cm^{-2}, a V_{oc} of 0.63 V, and a FF of 59.4%, resulting in a decreased PCE of 4.49%. This may be attributed to the fact that the ligands surrounding alloy NPs are insulators, which induce the barriers for charge transport in the interpenetrating network. High concentration of nanoalloys embedded in the BHJ active layer causes

more trapping sites for charge recombination. These results are consistent with those observed in TM-AFM images (Figure 2). Unlike $Au_{11}Ag_{89}$ nanoalloys, the $Au_{28}Ag_{72}$-fabricated solar cells exhibit a much lower photovoltaic performance (Figure S7a, Supporting Information) due to the interfacial barrier and dissimilarities in the morphologies of active layers. This could be related to the high tendency of the $Au_{28}Ag_{72}$ alloy aggregation, resulting in poor intermixing of the blend components (see Figure 2). The net result is to essentially retard the charge separation/transfer and thus give rise to the charge recombination of electron-hole pairs, leading to the mediocre J_{sc} and FF.[25] Nevertheless, the photovoltaic performance is still rather low in all cases with PCEs around 1.74–3.53%, where the low FF is indicative of inferior blend morphology, as supported by the TM-AFM results. Furthermore, the V_{oc} of $Au_{28}Ag_{72}$ is significantly lower (c.f. $Au_{11}Ag_{89}$, vide supra), falling sharply as the $Au_{28}Ag_{72}$ alloy concentration in the active layer increases due to trap-limited charge transport and trap-assisted recombination.[17,19,20] This viewpoint is further supported by UPS elaborated in the later section.

According to the BHJ devices fabricated with various concentrations of $Au_{11}Ag_{89}$ nanoalloys as shown in Figure 5c, very broad and panchromatic spectra over the entire excitation spectral range are obtained from IPCE measurements. The trend in the IPCE spectra correlates with those values of J_{sc}. Compared to the reference BHJ device, the results thus clearly show that incorporation of $Au_{11}Ag_{89}$ alloy NPs into the active layers causes more effective solar energy harvesting capability as well as the high charge transport mobility for improving the solar cell performance. The IPCE spectrum of active layer incorporation of 1% $Au_{11}Ag_{89}$ nanoalloys exceeds 65% in the 485–565-nm range and nearly 50% in the 430–630-nm range. The result also demonstrates that the photon wavelength for the current generation extends to 800 nm, as expected from the absorption spectrum of the active layer (Figure 3a). In addition, the spectral response enhancement is clearly observed in the range of 440–620-nm for all BHJ active layers blended with 1–10% $Au_{11}Ag_{89}$ bimetallic NPs.

2.5. UPS Studies

To explore the mechanisms leading to the improvement of devices comprising of AuAg nanoalloys, the energy levels of P3HT:PC_{61}BM films with and without alloy NPs were measured via UPS. **Figure 6**a depicts the UPS valence band spectra of reference P3HT:PC_{61}BM blend film and the corresponding films with 5% and 10% of $Au_{11}Ag_{89}$ alloy NPs. The HOMO spectrum of reference P3HT:PC_{61}BM film illustrated on the right side of Figure 6a is almost the same as that of pristine P3HT, which is consistent with the previous reports,[51–53] indicating that the reference film consists of a P3HT-rich region near the top surface. By incorporation of 5% or 10% $Au_{11}Ag_{89}$ nanoalloys into the reference films, the HOMO spectra exhibit a 0.3 eV shift toward higher binding energy. Additionally, as compared with the reference film, the secondary electron cutoff of blend with 10% of $Au_{11}Ag_{89}$ alloy NPs shifts toward high binding energy by 0.25 eV (from 17 eV to 17.25 eV), corresponding to the vacuum level shift at the interface. From the energy shift of the vacuum level and the HOMO spectra in UPS, the band diagrams are shown in the Figure 6b. The HOMO level of the reference film after the introduction of 10% of $Au_{11}Ag_{89}$ nanoalloys shows a downward shift by 0.3 eV with respect to the Fermi level. Since this HOMO feature belongs to P3HT, which is the donor in the photoactive layer, this offset will result in the enlargement of the energy difference between the HOMO level of donors and the LUMO level of acceptors. It has been established that the value of V_{oc} in BHJ solar cell is closely related to this energy level difference[17,54] and therefore the downward shift of HOMO level of donors would result in the V_{oc} increase in our BHJ solar cells with $Au_{11}Ag_{89}$ bimetallic NPs. On the other hand, the results of metal alloy with higher Au composition up to $Au_{28}Ag_{72}$ are quite different from the case of $Au_{11}Ag_{89}$.

Figure 6c displays the UPS spectra of P3HT:PC_{61}BM blended with 5% and 10% of $Au_{28}Ag_{72}$ nanoalloys. As compared with the spectrum of the reference film shown in Figure 6a, the HOMO levels of reference film with both 5% and 10% of $Au_{28}Ag_{72}$ alloy NPs are at the energy position close to that of reference film (0.9 eV below the Fermi level). Nevertheless,

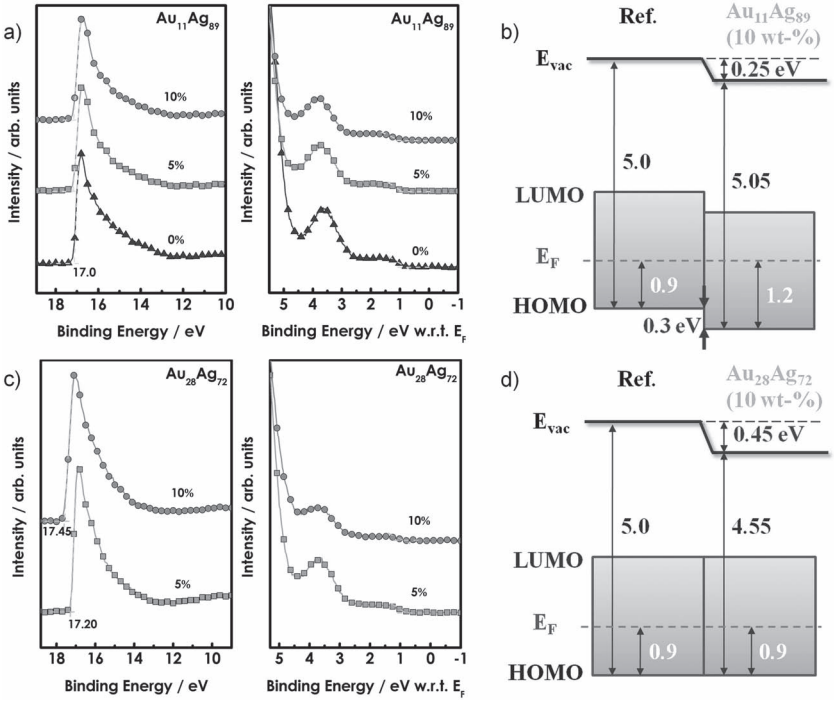

Figure 6. a) UPS spectra of P3HT:PC_{61}BM with incorporation of 0%, 5%, and 10% $Au_{11}Ag_{89}$ nanoalloys. b) Evolution of energy diagrams of P3HT:PC_{61}BM (Ref.) and the P3HT:PC_{61}BM with introducing of 10% $Au_{11}Ag_{89}$ nanoalloys. c) UPS spectra of P3HT:PC_{61}BM with incorporation of 5% and 10% $Au_{28}Ag_{72}$ nanoalloys. d) Evolution of energy diagrams of P3HT:PC_{61}BM (Ref.) and the P3HT:PC_{61}BM with introducing of 10% $Au_{28}Ag_{72}$ nanoalloys.

the secondary electron cutoff obviously shifts toward higher binding energy with blending of $Au_{28}Ag_{72}$ nanoalloys. The cutoff positions of 5% and 10% of $Au_{28}Ag_{72}$ nanoalloys are at 17.5 eV and 17.45 eV, respectively. Therefore, the energy difference between the vacuum level and the HOMO energy level of P3HT:PC_{61}BM with 10% $Au_{28}Ag_{72}$ bimetallic NPs decreases from 5 eV to 4.55 eV (Figure 6d), which is smaller than the typical ionization potential of P3HT (~5 eV). These results point out that the physical characteristics at the P3HT:PC_{61}BM film's surface, including electronic properties and morphology, might encounter significant changes after the mixture with $Au_{28}Ag_{72}$ alloy NPs, which is consistent with the findings in TM-AFM images (vide supra). Combinations of the UPS and TM-AFM images show that the poor performance of devices with $Au_{28}Ag_{72}$ nanoalloys might be due to the adverse morphology of the surfaces, resulting in exciton loss, geminate charge recombination, and poor charge mobility.[19,22,25]

3. Conclusion

In summary, we present a simple and versatile method for generating large and monodispersed of AuAg alloy NPs in organic phase, for which the mechanism of production is also elaborated in detail. Importantly, Au/Ag precursors' molar ratios are the way of tailoring the optical properties of nanoalloys. Simultaneous enhancement in J_{sc}, V_{oc}, FF, and IPCE can be achieved in high-performance BHJ solar cells by simply incorporation of 1% $Au_{11}Ag_{89}$ nanoalloys into the active layers, resulting in a compelling device-performance of 31% PCE enhancement, along with a PCE of up to 4.73% in comparison to that of the control standard device of P3HT:PC_{61}BM fabricated and tested under the same conditions. The results suggest that metal NPs in the active layer could serve as scattering centers with tunable plasmon resonances for increasing the fraction of incoming light absorption, as well as improving the charge transport and series resistance. Among the as-prepared Au, Ag, $Au_{28}Ag_{72}$ and $Au_{11}Ag_{89}$ alloy NPs, $Au_{11}Ag_{89}$ exhibits the most promising high-performance metallic additive than the rest. The local field enhancement from the narrow band plasmon resonances is not the dominant mechanism in our study. Instead, the multiple light scattering leads to increase optical path length within the active layer and is therefore responsible for the enhancement of the PCE. This study may thus open up the possibility of a new route for fabricating various species of large size of nanoalloys to improve the design of efficient BHJ solar cells.

4. Experimental Section

Materials: Gold acetate ($Au(ac)_3$, Alfa Aesar, 99.9%), silver nitrate ($AgNO_3$, Aldrich, 99.9%), trioctylphosphine (TOP, Aldrich, 90%), octyl ether (Tokyo Chemical Industry, 95%), 1,2-dodecanediol (DDD, Aldrich, 90%), oleylamine (OAm, Acros, approximate C18-content 80-90%) and oleic acid (OAc, Aldrich, 90%), poly(3,4-ethylenedioxythiophene) poly(styrenesulfonate) (PEDOT:PSS, Baytron P VP AI 4083 from H. C. Starck), regioregular poly(3-hexylthiophene) (P3HT, Rieke Metals), and [6,6]-phenyl-C_{61}-butyric acid methyl ester (PC_{61}BM, Nano-C). All of the chemical reagents and solvents were purchased from commercial sources and used as received without further purification.

Synthesis of Ag NPs: For the synthesis of Ag NPs, $AgNO_3$ (50 mg), DDD (200 mg), TOP (0.7 mL) OAc (1 mL) and OAm (3 mL), were mixed with octyl ether (6 ml) in reaction bottle under N_2. The reaction mixture was heated to 200 °C at heating rate of ~15 °C min^{-1} and refluxed for 40 min. After that, the heating source was removed and the mixture was cooled to the room temperature. The resulting product was precipitated by adding methanol and separated by centrifugation. Finally, the Ag NPs were stored in 1,2-dichlorobenzene (DCB).

One-Pot Synthesis of $Au_{11}Ag_{89}$ and $Au_{28}Ag_{72}$ Alloy NPs: The synthetic procedures were similar to that of synthesis of Ag NPs. In the synthesis of $Au_{11}Ag_{89}$ nanoalloys, the amount of DDD, TOP, OAc, OAm and octyl ether were the same as the initial feed. However, the weight of $AgNO_3$ was deceased to 40 mg. After that, $Au(ac)_3$ (15 mg) was added into the above mixture in a reaction bottle. For the synthesis of $Au_{28}Ag_{72}$ nanoalloys, the weight of $AgNO_3$ was deceased to 35 mg and the content of $Au(ac)_3$ was up increased to 20 mg. In addition to these mentioned above, all of other parameters and procedures were the same as described in details of synthesis of Ag NPs. As the reaction mixture of Ag and AuAg NPs were heated to 100–110 °C, the reaction solution (100 µL) was draw out, followed by add into hexane (1.9 mL). Finally, the UV-vis spectra of complexation conditions of the above solutions were recorded (Figure S1a, Supporting Information). Also, the complexation condition of AuAg NPs prepared in the absence of TOP and Ag-TOP complex were obtained through the above procedure.

Synthesis of Au NPs: Au NP solution was prepared using procedures described previously.[55]

Measurement and Characterization: The steady-state absorption and emission spectra were recorded on a Hitachi U-4100 spectrophotometer and an Edinburgh FS920 fluorimeter, respectively. Both the wavelength-dependent excitation and the emission response of the fluorimeter were calibrated. The TEM images were obtained by JEOL JEM-1230 and Philips/FEI Tecnai 20 G^2 S-Twin transmission electron microscope. The compositional analysis was performed by using energy-dispersive spectrometer on Philips/FEI Tecnai 20 G^2 S-Twin transmission electron microscope. The TM-AFM images were taken on a NanoScope IIIa controller (Veeco Metrology Group/Digital Instruments). Time-resolved spectroscopic measurements were carried out by means previously reported elsewhere in detail.[56] In brief words, sub-ns to ns time-resolved studies were performed using a time-correlated single photon counting (TCSPC) system (OB-900L lifetime spectrometer, Edinburgh) with the excitation light from second harmonic generation (SHG, at 400 nm) of pulse-selected femtosecond laser pulses at 800 nm (Tsunami and Model 3980 pulse picker, Spectra-Physics). The fluorescence was collected at a right angle with respect to the pump beam path and passed through a polarizer, setting the polarization at the magic angle (54.7°) with respect to the pump polarization, and located in front of the detector to eliminate anisotropy. The temporal resolution, after partial removal of the instrument time-broadening, is ~30 ps. The data were fitted to the sum of exponential functions convoluted with the instrument response function, which was determined by measuring the Raman scattering signal. The valence-band ultraviolet photoemission spectra (UPS) were measured via He I (21.2 eV) photons as excitation sources with a base pressure at the order of 10^{-10} Torr. The photoelectrons emitted from the sample were recorded by a hemispherical analyzer with an overall resolution of 0.05 eV, as determined from the width of the Fermi step measured on a gold substrate cleaned by Ar ion sputter. The HOMO levels of thin films were defined by extrapolating the edges of the HOMO peaks down to the background of the UPS spectra. The vacuum levels of the samples were derived from the onset of the UPS spectra at the high binding energy sides. The P3HT:PC_{61}BM blend films for photoemission experiments with and without AuAg alloy NPs were prepared with the same conditions as those used in the devices fabrication and were then transferred into vacuum chambers for spectroscopy measurements.

Solar Cell Device Fabrication and Characterization: BHJ solar cells were fabricated with the device configuration of ITO/PEDOT:PSS/P3HT:PC_{61}BM:metal NPs/Ca/Al. Optimized solar cell devices used in this study were prepared by dissolving P3HT and PC_{61}BM in DCB in a weight ratio of 1:1 with a P3HT concentration of 17 mg ml^{-1} containing

0–10% metal NPs. Prior to use, patterned ITO-coated glass substrates (15 Ω/square) were successively cleaned by ultrasonication in 1% neutral detergent in water, then deionized water, followed by acetone and finally 2-propanol for 20 min each. The substrates were then dried and oxygen plasma treatment immediately prior to the deposition of a 35-nm-thick layer of PEDOT:PSS, as verified by a Dektak 3030 profilometer. Deposition of the PEDOT:PSS layer was followed by baking at 140 °C for 20 min. Substrates were subsequently transferred to an inert N_2-filled glove box (< 0.1 ppm O_2 and H_2O), and the active layer was spin-coated onto the PEDOT:PSS layer. The wet film was slowly dried in a covered Petri dish for a certain time and subsequently annealed at 150 °C for 10 min in the glove box. The thicknesses of the P3HT:PC_{61}BM composite films were adjusted to ~100–170 nm by controlling the spin-coating rate. The coated substrates were then transferred to a thermal evaporator and evacuated to $\leq 1 \times 10^{-6}$ Torr before a 30-nm-thick calcium layer followed by a 100-nm aluminium electrode layer were deposited. The thin interfacial layer of calcium has been reported to enhance the fill factor of the devices.[2–4,6–8,11] The fabricated device was encapsulated in a nitrogen-filled glove box with UV epoxy and cover glass. The *J–V* curves were measured with a Newport-Oriel AM 1.5 G light source operating at 100 mW cm^{-2} and independently cross-checked using a 300-W AM 1.5 G source operating at 100 mW cm^{-2} for verification. The light intensity was determined by a monosilicon detector (with KG-5 visible color filter) calibrated by the National Renewable Energy Laboratory (NREL) to minimize spectral mismatch. The IPCE spectra were measured using a lock-in amplifier with a current preamplifier under short-circuit conditions. The devices were illuminated by monochromatic light from a xenon lamp passing through a monochromator with a typical intensity of 30 μW. A calibrated monosilicon diode with known spectral response was used as a reference.

Supporting Information

Supporting Information is available from the Wiley Online Library or from the author.

Acknowledgements

H.-C.C. and S.-W.C. contributed equally to this work. This work was supported by the National Science Council and Ministry of Economic Affairs of Taiwan (NSC 100-2119-M-002-008). The authors thank Prof. Hsing-Wen Wang and Po-Hsiung Chen, National Yang-Ming University, for the diffuse reflectance spectra measurements and analysis.

Received: January 24, 2012
Revised: May 12, 2012
Published online: June 4, 2012

[1] J. Peet, A. J. Heeger, G. C. Bazan, *Acc. Chem. Res.* **2009**, *42*, 1700.
[2] J. Hou, H.-Y. Chen, S. Zhang, R. I. Chen, Y. Yang, Y. Wu, G. Li, *J. Am. Chem. Soc.* **2009**, *131*, 15586.
[3] H.-C. Chen, I-C. Wu, J.-H. Hung, F.-J. Chen, I-W. P. Chen, Y.-K. Peng, C.-S. Lin, C.-h. Chen, Y.-J. Sheng, H.-K. Tsao, P.-T. Chou, *Small* **2011**, *7*, 1098.
[4] Q. Peng, X. Liu, D. Su, G. Fu, J. Xu, L. Dai, *Adv. Mater.* **2011**, *23*, 4554.
[5] P. M. Beaujuge, J. M. J. Fréchet, *J. Am. Chem. Soc.* **2011**, *133*, 20009.
[6] M. Zhang, X. Guo, X. Wang, H. Wang, Y. Li, *Chem. Mater.* **2011**, *23*, 4264.
[7] Y. Liang, Z. Xu, J. Xia, S.-T. Tsai, Y. Wu, G. Li, C. Ray, L. Yu, *Adv. Mater.* **2010**, *22*, E135.
[8] H.-Y. Chen, J. Hou, S. Zhang, Y. Liang, G. Yang, Y. Yang, L. Yu, Y. Wu, G. Li, *Nat. Photonics* **2009**, *3*, 649.
[9] Z. He, C. Zhong, X. Huang, W.-Y. Wong, H. Wu, L. Chen, S. Su, Y. Cao, *Adv. Mater.* **2011**, *23*, 4636.
[10] I-C. Wu, C.-H. Lai, D.-Y. Chen, C.-W. Shih, C.-Y. Wei, B.-T. Ko, C. Ting, P.-T. Chou, *J. Mater. Chem.* **2008**, *18*, 4297.
[11] X. Fan, C. Cui, G. Fang, J. Wang, S. Li, F. Cheng, H. Long, Y. Li, *Adv. Funct. Mater.* **2012**, *22*, 585.
[12] Z. Tang, L. M. Andersson, Z. George, K. Vandewal, K. Tvingstedt, P. Heriksson, R. Kroon, M. R. Andersson, O. Inganäs, *Adv. Mater.* **2012**, *24*, 554.
[13] I. Gur, N. A. Fromer, C. P. Chen, A. G. Kanaras, A. P. Alivisatos, *Nano Lett.* **2007**, *7*, 409.
[14] H.-C. Chen, C.-W. Lai, I-C. Wu, H.-R. Pan, I-W. P. Chen, Y.-K. Peng, C.-L. Liu, C.-h. Chen, P.-T. Chou, *Adv. Mater.* **2011**, *23*, 5451.
[15] B. Sun, E. Marx, N. C. Greenham, *Nano Lett.* **2003**, *3*, 961.
[16] Y. Wu, G. Zhang, *Nano Lett.* **2010**, *10*, 1628.
[17] C. J. Brabec, A. Cravino, D. Meissner, N. S. Sariciftci, T. Fromherz, M. T. Rispens, L. Sanchez, J. C. Hummelen, *Adv. Funct. Mater.* **2001**, *11*, 374.
[18] D. Jarzab, F. Cordella, J. Gao, M. Scharber, H.-J. Egelhaaf, M. A. Loi, *Adv. Energy Mater.* **2011**, *1*, 604.
[19] L. J. A. Koster, M. Kemerink, M. M. Wienk, K. Maturová, R. A. J. Janssen, *Adv. Mater.* **2011**, *23*, 1670.
[20] K. Vandewal, K. Tvingstedt, A. Gadisa, O. Inganäs, J. V. Manca, *Nat. Mater.* **2009**, *8*, 904.
[21] Z. Li, F. Gao, N. C. Greenham, C. R. McNeill, *Adv. Funct. Mater.* **2011**, *21*, 1419.
[22] C. J. Brabec, M. Heeney, I. McCulloch, J. Nelson, *Chem. Soc. Rev.* **2011**, *40*, 1185.
[23] Y. D. Park, J. K. Park, J. H. Seo, J. D. Yuen, W. H. Lee, K. Cho, G. C. Bazan, *Adv. Energy Mater.* **2011**, *1*, 63.
[24] J. K. Lee, W. L. Ma, C. J. Brabec, J. Yuen, J. S. Moon, J. Y. Kim, K. Lee, G. C. Bazan, A. J. Heeger, *J. Am. Chem. Soc.* **2008**, *130*, 3619.
[25] K. Maturová, S. S. van Bavel, M. M. Wienk, R. A. J. Janssen, M. Kemerink, *Adv. Funct. Mater.* **2011**, *21*, 261.
[26] J. A. Schuller, E. S. Barnard, W. Cai, Y.-C. Jun, J. S. White, M. L. Brongersma, *Nat. Mater.* **2010**, *9*, 193.
[27] H. A. Atwater, A. Polman, *Nat. Mater.* **2010**, *9*, 205.
[28] M. Rycenga, C. M. Cobley, J. Zeng, W. Li, C. H. Moran, Q. Zhang, D. Qin, Y. Xia, *Chem. Rev.* **2011**, *111*, 3669.
[29] M.-C. Daniel, D. Astruc, *Chem. Rev.* **2004**, *104*, 293.
[30] M. H. Huang, P.-H. Lin, *Adv. Funct. Mater.* **2012**, *22*, 14.
[31] M. Heo, H. Cho, J.-W. Jung, J.-R. Jeong, S. Park, J. Y. Kim, *Adv. Mater.* **2011**, *23*, 5689.
[32] J.-L. Wu, F.-C. Chen, Y.-S. Hsiao, F.-C. Chien, P. Chen, C.-H. Kuo, M. H. Huang, C.- S. Hsu, *ACS Nano* **2011**, *5*, 959.
[33] D. D. S. Fung, L. Qiao, W. C. H. Choy, C. Wang, W. E. I. Sha, F. Xie, S. He, *J. Mater. Chem.* **2011**, *21*, 16349.
[34] D. H. Wang, K. H. Park, J. H. Seo, J. Seifter, J. H. Jeon, J. K. Kim, J. H. Park, O O. Park, A. J. Heeger, *Adv. Energy Mater.* **2011**, *1*, 766.
[35] C. C. D. Wang, W. C. H. Choy, C. Duan, D. D. S. Fung, W. E. I. Sha, F.-X. Xie, F. Huang, Y. Cao, *J. Mater. Chem.* **2012**, *22*, 1206.
[36] C.-H. Kim, S.-H. Cha, S. C. Kim, M. Song, J. Lee, W. S. Shin, S.-J. Moon, J. H. Bahng, N. A. Kotov, S.-H Jin, *ACS Nano* **2011**, *5*, 3319.
[37] M. Xue, L. Li, B. J. T. de Villers, H. Shen, J. Zhu, Z. Yu, A. Z. Stieg, Q. Pei, B. J. Schwartz, K. L. Wang, *Appl. Phys. Lett.* **2011**, *98*, 253302.
[38] C. Wang, H. Yin, R. Chan, S. Peng, S. Dai, S. Sun, *Chem. Mater.* **2009**, *21*, 433.
[39] C. Wang, S. Peng, R. Chan, S. Sun, *Small* **2009**, *5*, 567.
[40] M. S. Shore, J. Wang, A. C. Johnston-Peck, A. L. Oldenburg, J. B. Tracy, *Small* **2011**, *7*, 230.
[41] V. E. Ferry, J. N. Munday, H. A. Atwater, *Adv. Mater.* **2010**, *22*, 4794.

[42] G. Konstantatos, E. H. Sargent, *Nat. Nanotechnol.* **2010**, *5*, 391.
[43] V. K. LaMer, R. H. Dinegar, *J. Am. Chem. Soc.* **1950**, *72*, 4847.
[44] K. Ahrenstorf, H. Heller, A. Kornowski, J. A. C. Broekaert, H. Weller, *Adv. Funct. Mater.* **2008**, *18*, 3850.
[45] M. Nakaya, M. Kanehara, T. Teranishi, *Langmuir* **2006**, *22*, 3485.
[46] E. V. Shevchenko, D. V. Talapin, H. Schnablegger, A. Kornowski, Ö. Festin, P. Svedlindh, M. Haase, H. Weller, *J. Am. Chem. Soc.* **2003**, *125*, 9090.
[47] S. Auer, D. Frenkel, *Nature* **2001**, *409*, 1020.
[48] J.-H. Liu, A.-Q. Wang, Y.-S. Chi, H.-P. Lin, C.-Y. Mou, *J. Phys. Chem. B* **2005**, *109*, 40.
[49] S. Liu, G. Chen, P. N. Prasad, M. T. Swihart, *Chem. Mater.* **2011**, *23*, 4098.
[50] G. Li, V. Shrotriya, J. Huang, Y. Yao, T. Moriarty, K. Emery, Y. Yang, *Nat. Mater.* **2005**, *4*, 864.
[51] Y. Vaynzof, D. Kabra, L. Zhao, L. L. Chua, U. Steiner, R. H. Friend, *ACS Nano* **2011**, *5*, 329.
[52] Z. Xu, L.-M. Chen, M.-H. Chen, G. Li, Y. Yang, *Appl. Phys. Lett.* **2009**, *95*, 013301.
[53] Z. Xu, L.-M. Chen, G. Yang, C.-H. Huang, J. Hou, Y. Wu, G. Li, C.-S. Hsu, Y. Yang, *Adv. Funct. Mater.* **2009**, *19*, 1227.
[54] P. W. M. Blom, V. D. Mihailetchi, L. J. A. Koster, D. E. Markov, *Adv. Mater.* **2007**, *19*, 1551.
[55] H. Hiramatsu, F. E. Osterloh, *Chem. Mater.* **2004**, *16*, 2509.
[56] P.-T. Chou, S.-C. Pu, Y.-M. Cheng, W.-S. Yu, Y.-C. Yu, F.-T. Hung, W.-P. Hu, *J. Phys. Chem. A* **2005**, *109*, 3777.